

Second-order artifact overwhelming the third-order signal in 2D Raman-THz spectroscopy of non-centrosymmetric materials

Seyyed Jabbar Mousavi^{1,2,*}, Megan F. Biggs³, Jeremy A. Johnson³, Peter Hamm¹ and Andrey Shalit^{1,*}

¹*Department of Chemistry, University of Zurich, Winterthurerstrasse 190,*

CH-8057 Zurich, Switzerland; email: andrey.shalit@chem.uzh.ch

²*Institute of Applied Physics, University of Bern, Sidlerstrasse 5,
3012 Bern, Switzerland; email: jabbar.mousavi@unibe.ch and*

³*Department of Chemistry and Biochemistry, Brigham Young University, Provo, Utah 84602, USA*

(Dated: July 15, 2024)

Through comprehensive data analysis, we demonstrate that a second-order artifact contributes significantly to the measured signal in 2D Raman-THz spectroscopy of non-centrosymmetric materials. We confirm that by measuring the 2D Raman-THz response of a beta barium borate (BBO) crystal, a well-known $\chi^{(2)}$ active sample. More importantly, we show that this strong second-order artifact can be effectively suppressed by implementing a special detection scheme. By doing so, we successfully isolate the desired third-order nonlinear response. Our experimentally recovered 2D Raman-THz signal for an x-cut BBO crystal reveals a distinct cross-peak feature, whose frequency position suggests the presence of phonon-phonon coupling within this crystal. Our study emphasizes the critical significance of considering second-order nonlinear responses when conducting 2D THz experiments involving non-centrosymmetric samples.

I. INTRODUCTION

Two-dimensional (2D) THz spectroscopy intends to measure the third-order nonlinear signal, giving useful insights into the dynamics and coupling of low-frequency modes in the THz frequency range in condensed-phase molecular systems.¹⁻⁵ Recently, the application of this technique was further expanded to explore the correlation and dynamics of rotational degrees of freedom in gas-phase molecules, revealing a multidimensional rotational spectroscopy.⁶⁻⁸ In two-pulse 2D THz experiment on non-centrosymmetric materials, $\chi^{(2)}$ nonlinear susceptibility can also contribute to the nonlinear signal.⁹ Various second-order contributions, with characteristic spectral features, originating from second harmonic generation (SHG), and optical rectification (OR) processes have been previously reported in 2D THz spectra of non-centrosymmetric materials.^{2,3,10,11}

For example, Elsaesser and co-workers studied intersubband transitions in GaAs/AlGaAs semiconductor quantum wells using two-pulse 2D THz spectroscopy.^{12,13} In addition to the third-order pump-probe and photon echo signals, they also observed second-order contributions to the 2D THz spectrum. The observed $\chi^{(2)}$ features were assigned to difference-frequency mixing in the bulk GaAs substrate. Nelson and co-workers investigated nonlinear responses of magnons and their correlations in an antiferromagnetic crystal, YFeO₃. They also observed that the second-order signals, including SHG and THz rectification (TR) peaks, originated from sum- and difference-frequency mixing of the magnons, respectively, contribute to the measured 2D THz spectra.¹¹ In a very recent 2D THz experiment on ZnTe, it has been shown that second-order contributions, such as rectified nonlinearities and second harmonic signals arising from the electro-optic sampling in the detection crystal, known as artifacts of the detection scheme, can also contaminate

2D spectra collected in a collinear geometry.¹⁴

Hybrid spectroscopies with two complementary pulse sequences of 2D Raman-THz-THz (2D RTT)¹⁵⁻¹⁹ and 2D THz-THz-Raman (2D TTR)²⁰⁻²⁴ are alternative approaches for performing 2D experiments in the THz frequency range. In this work, we present a new observation on how second-order artifacts can dominate the third-order signal in 2D Raman-THz experiments involving $\chi^{(2)}$ active samples. These artifacts are effectively linear (i.e., 1D) responses and overwhelm the measured nonlinear signal, potentially leading to misleading interpretations.

We will first present our measured 2D Raman-THz data for an x-cut BBO nonlinear crystal. By analyzing the measured data, we confirm that the observed features originated from the second-order contribution rather than the third-order response of the sample. We also introduce the origin of this contribution and explain why the differential chopping detection scheme is insufficient to isolate the third-order signal in such cases. Finally, with the goal of recovering the real 2D Raman-THz response of the BBO crystal, we measure the x-cut BBO signal using a special detection scheme based on the work of Johnson *et al.*²⁵ and Brunner *et al.*²⁶. Our data provide experimental evidence suggesting the presence of phonon-phonon coupling within the BBO crystal.

II. METHODS

The experimental setup for 2D Raman-THz spectroscopy has been described in detail before.¹⁵ Briefly, the output of an amplified Ti:sapphire laser system, operating at a center wavelength of 800 nm, pulse duration of 110 fs, and repetition rate of 5 kHz, is divided into Raman and THz branches using a beamsplitter. The beam used for the THz branch is further split into two beams:

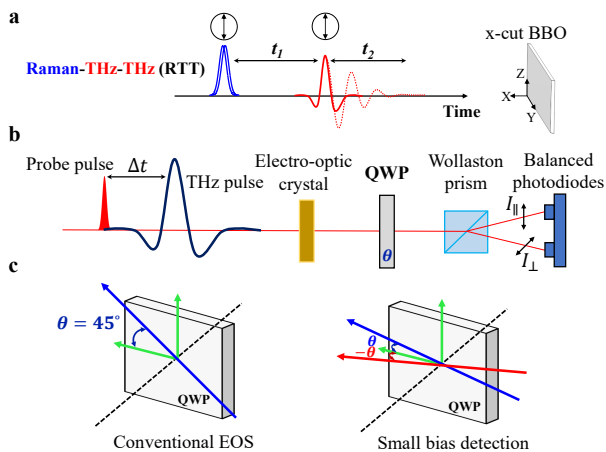


FIG. 1: a) Schematic of the 2D Raman-THz spectroscopy with RTT pulse sequence. The polarization of the Raman and THz pulses is shown in the circles. b) Electro-optic sampling (EOS) detection scheme. c) Angle of the quarter-wave plate at 45° in conventional EOS (left panel), and two small opposite angles around zero in small bias detection scheme (right panel).

one for THz generation and the other for THz detection (gated beam). All three laser beams have parallel polarizations, aligned parallel to the crystallographic z-axis of BBO as shown in Fig. 1a. Broadband THz pulses are generated via optical rectification in a $200\ \mu\text{m}$ -thick (110) GaP crystal. Before reaching the GaP crystal, the THz generation beam is modulated using a mechanical chopper operating at a frequency of one-quarter of the laser repetition rate (1.25 kHz). The generated THz pulses are first focused onto the sample and then directed towards the detection crystal (a $200\ \mu\text{m}$ -thick GaP crystal) using two custom-made aluminum elliptical mirrors. The Raman pump pulses with energies up to $40\ \mu\text{J}$ are first modulated at half of the laser repetition rate (2.5 kHz) and subsequently focused onto the sample. The temporal delays t_1 , the delay between the Raman pump and generated THz field, and t_2 , the delay between THz generation and detection, are controlled by two step-scan motors. 2D Raman-THz-THz (RTT) pulse sequence is shown schematically in Fig. 1a. The emitted signal (red dotted line shown in Fig. 1a) is focused onto the detection crystal and measured using conventional electro-optic sampling (EOS) scheme (see Fig. 1b). To prevent water vapor absorption, the entire THz section of the experimental setup, including the THz generation and detection components, is enclosed within a nitrogen-purged box.

We also employed an alternative experimental approach, known as the small bias detection scheme,^{25–27} to effectively isolate the very weak third-order nonlinear signal from a strong second-order contribution caused by imperfect balancing in the 2D Raman-THz experiment on the x-cut BBO crystal. As previously mentioned, in

the conventional EOS detection scheme (see Fig. 1b), the angle of the QWP is typically set to 45° (see Fig. 1c-left panel), converting the linearly polarized probe beam into circular polarization which is subsequently split by the Wollaston prism into two *s* and *p* polarization components with equal intensity. In the small bias detection scheme, this angle is set to a small angle close to 0° , which effectively reduces the optical bias from the usual setting.²⁵ In this configuration, a significant portion of the probe beam intensity, whose polarization is parallel to the probe beam polarization (I_{\parallel}), is directed towards one of the photodiodes. Balance detection can then be achieved by adjusting a variable attenuator located in front of that photodiode, thereby attenuating the main polarization component. The bias detection scheme has the same effect on increasing the sensitivity of the THz detection as the Brewster windows scheme that we had introduced previously,²⁸ but as we will see, introduces an additional tuning parameter that allows one to suppress the second-order artifact.

III. RESULTS AND DISCUSSION

A. 2D Raman-THz spectroscopy of x-cut BBO crystal

Figure 2a shows the 2D time domain response measured using the RTT pulse sequence and detected by conventional EOS, for a $100\ \mu\text{m}$ thick x-cut BBO crystal. As can be seen, a long-lived oscillatory feature along both t_1 and t_2 axes dominates the measured signal in the time domain. Figure 2b shows the absolute value of the 2D Fourier transformation of the data in Fig. 2a. Three main peaks with frequencies of 2.18 THz, 2.85 THz, and 3.5 THz are observed along the f_1 frequency axis. The observed features appear to climb up and align along the diagonal line, accompanied by a splitting of these features that follows the spectral shape of the instrument response function (IRF), as discussed in Ref. 17. It has been previously shown that the convolution of molecular response with the IRF strongly affects the 2D Raman-THz response in terms of spectral shape, intensity, and frequency position.¹⁷ IRF has two nodal lines, one on the diagonal and the other along the f_1 axis, suppressing diagonal peaks and those along the f_1 axis with $f_2 = 0$. In the next section, we will prove that the observed features in Fig. 2b are $\chi^{(2)}$ artifacts originating from imperfect balancing in the conventional EOS detection scheme.

B. THz signal at arbitrary quarter-wave plate angle

In the conventional electro-optic sampling detection scheme, where the quarter-wave plate is oriented at $\theta = 45^\circ$, the intensities of the two orthogonal polarization

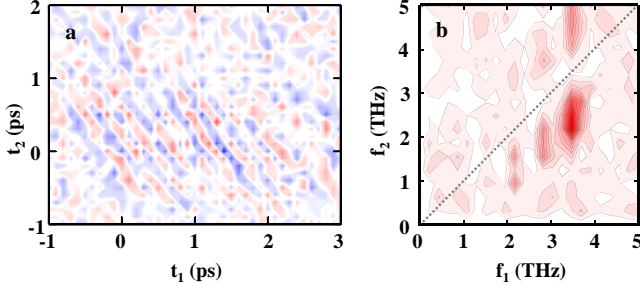


FIG. 2: a) 2D time domain response measured using the RTT pulse sequence and detected by conventional EOS, for the x-cut BBO crystal. b) Absolute value of the 2D Fourier transformation for the data shown in panel (a).

components at the balanced photodiodes are:²⁹

$$I_{\perp} = \frac{I_0}{2} (1 + \sin(\phi)) \quad (1)$$

$$I_{\parallel} = \frac{I_0}{2} (1 - \sin(\phi)) \quad (2)$$

where I_0 is the probe beam intensity, and ϕ is the phase retardation experienced by the probe beam due to the THz electric field. As a result, the normalized EOS signal, which is obtained as the intensity difference between two balanced photodiodes is:²⁹

$$I_s = \frac{I_{\perp} - I_{\parallel}}{I_0} = \sin(\phi). \quad (3)$$

However, when a quarter-wave plate is oriented at an arbitrary angle θ , the intensities of the two orthogonal polarization components are given by²⁶

$$I_{\perp}(\phi, \theta) = \frac{I_0}{2} \times \{1 + \sin(2\theta) \sin(\phi) - \cos^2(2\theta) \cos(\phi)\} \quad (4)$$

$$I_{\parallel}(\phi, \theta) = \frac{I_0}{2} \times \{1 - \sin(2\theta) \sin(\phi) + \cos^2(2\theta) \cos(\phi)\}. \quad (5)$$

Here for simplicity, we neglect the small contributions from phase retardations due to the strain-induced birefringence of the detection crystal and the scattering background. To achieve balanced detection in the small bias detection scheme, the main polarization component (I_{\parallel}) needs to be attenuated by a factor $T \ll 1$:

$$T = \frac{\sin^2(2\theta)}{1 + \cos^2(2\theta)} \quad (6)$$

in which case we have ($I_{\perp} = TI_{\parallel}$) when $\phi = 0$. The normalized balanced difference signal then is:

$$\begin{aligned} I_s(\phi, \theta) &= \frac{I_{\perp}(\phi, \theta) - TI_{\parallel}(\phi, \theta)}{I_{\perp}(0, \theta) + TI_{\parallel}(0, \theta)} \\ &= \frac{1}{\sin^2(2\theta)} \{ (1 + T)(\sin(2\theta) \sin(\phi) - \cos^2(2\theta) \cos(\phi)) - T + 1 \}. \end{aligned} \quad (7)$$

For assuming a small THz-induced phase retardation ($\phi \ll 1$), we can Taylor expand $\sin(\phi)$ and $\cos(\phi)$ up to second order, simplifying equation 7:

$$\begin{aligned} I_s(\phi, \theta) &= \frac{1}{\sin^2(2\theta)} \{ (1 + T)(\sin(2\theta)\phi - \cos^2(2\theta)(1 - \frac{\phi^2}{2})) - T + 1 \} \end{aligned} \quad (8)$$

In addition to balanced detection, we employ a differential chopping detection scheme in order to isolate the nonlinear signal from other undesired signals arising from individual pulses, such as scattering effects and optical rectification. The implementation of the two-chopper scheme enables us to acquire four distinct measurements, denoted as $I_{t,r}$, where the subscripts t and r represent the states of the THz and Raman choppers, respectively (1 or 0):

$$\begin{aligned} I_{1,1} &= THz_{On} Raman_{On} \\ I_{1,0} &= THz_{On} Raman_{Off} \\ I_{0,1} &= THz_{Off} Raman_{On} \\ I_{0,0} &= THz_{Off} Raman_{Off} \end{aligned}$$

The measured 2D Raman-THz signal is then calculated according to:

$$S = ((I_{1,1} - I_{1,0}) - (I_{0,1} - I_{0,0})) \quad (9)$$

Here, we first provide a mathematical demonstration of how second-order contributions overwhelms the signal in non-centrosymmetric materials, and subsequently validate it experimentally. Using equation 8 for the normalized balanced difference signal in EOS, the four individual signals measured with our two-chopper scheme can be written as:

$$I_{0,0}(0, \theta) = \frac{1}{\sin^2(2\theta)} \{ (1 + T)(-\cos^2(2\theta)) - T + 1 \} \quad (10)$$

$$\begin{aligned} I_{1,0}(\phi_{THz}, \theta) &= \frac{1}{\sin^2(2\theta)} \{ (1 + T)(\sin(2\theta)\phi_{THz} - \cos^2(2\theta)(1 - \frac{\phi_{THz}^2}{2})) - T + 1 \} \end{aligned} \quad (11)$$

$$\begin{aligned} I_{0,1}(\phi_{Raman}, \theta) &= \frac{1}{\sin^2(2\theta)} \{ (1 + T)(\sin(2\theta)\phi_{Raman} - \cos^2(2\theta)(1 - \frac{\phi_{Raman}^2}{2})) - T + 1 \} \end{aligned} \quad (12)$$

$$\begin{aligned}
I_{1,1}(\phi_{THzRaman}, \theta) = & \frac{1}{\sin^2(2\theta)} \{ (1+T)(\sin(2\theta)\phi_{THzRaman} \\
& - \cos^2(2\theta)(1 - \frac{\phi_{THzRaman}^2}{2}) \\
& - T + 1 \}
\end{aligned} \tag{13}$$

where ϕ_{THz} and ϕ_{Raman} are phase retardations due to the THz excitation pulse transmitted through the sample, and the Raman-induced $\chi^{(2)}$ process in the sample (BBO crystal), respectively. The term $\phi_{THzRaman}$ represents the sum of the phase retardations induced by THz (ϕ_{THz}) and Raman (ϕ_{THz}) pulses, along with the contribution from the desired third-order nonlinear signal ϕ_{3rdNL} ($\chi^{(3)}$ response):

$$\phi_{THzRaman} = \phi_{THz} + \phi_{Raman} + \phi_{3rdNL} \tag{14}$$

Using the above definitions for the individual signals, the measured 2D Raman-THz signal can be calculated as follows:

$$\begin{aligned}
S = & \frac{1}{\sin^2(2\theta)} \{ (1+T)(\sin(2\theta)\phi_{3rdNL} \\
& + \cos^2(2\theta)(\phi_{THz}\phi_{Raman} + \phi_{THz}\phi_{3rdNL} \\
& + \phi_{Raman}\phi_{3rdNL} + \frac{(\phi_{3rdNL})^2}{2}) \}
\end{aligned} \tag{15}$$

Theoretically, when the angle of the quarter-wave plate is set to 45° , the $\cos^2(2\theta)$ -terms become zero and the signal should be:

$$S = \frac{1+T}{\sin(2\theta)} \phi_{3rdNL} \tag{16}$$

However, in practice, there is always some leakage due to the imperfections in the probe beam polarization and the polarizing optics. As we show in this paper, this issue becomes particularly crucial when trying to measure the extremely weak $\chi^{(3)}$ signals of non-centrosymmetric materials ($\chi^{(2)}$ active samples). When the Raman-induced THz field ϕ_{Raman} is present, the $\phi_{THz}\phi_{Raman}$ term (called as product field) is much larger than any of other terms in the equation 15. Therefore, signal S is dominated by the product field:

$$S \propto \phi_{THz}\phi_{Raman} \tag{17}$$

regardless of the angle θ of the quarter-wave plate, making it impossible for the conventional EOS detection scheme to isolate the weak $\chi^{(3)}$ signal from the strong $\chi^{(2)}$ artifact.

Figures 3a and 3b displays the 2D plots in the time domain for the THz field transmitted through a $100 \mu\text{m}$ thick x-cut BBO crystal, ϕ_{THz} , and Raman-induced THz field, ϕ_{Raman} . Both are plotted in a 2D representation, with the delay times as they are given by the experimental configuration, but they are 1D signals. The inset in Fig. 3b shows the Fourier transformation of 1D cut along

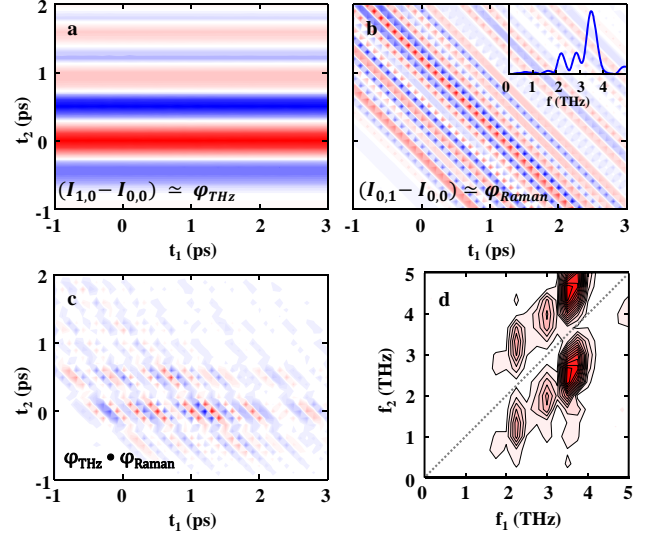


FIG. 3: 2D plots in the time domain for a) the THz field transmitted through the $100 \mu\text{m}$ thick x-cut BBO crystal, denoted as ϕ_{THz} , and b) Raman-induced THz field, labeled as ϕ_{Raman} . The inset in Fig. 3b shows the Fourier transformation of 1D cut along t_1 axis for ϕ_{Raman} . Multiplication of the transmitted THz field through the $100 \mu\text{m}$ thick x-cut BBO crystal and Raman-induced THz field, called as product field ($\phi_{THz}\phi_{Raman}$), in c) the time and d) frequency domains.

t_1 axis for the data shown in Fig. 3b. This figure demonstrates that when the Raman pulse hits the BBO sample, it generates a THz field, called as Raman-induced THz field, ϕ_{Raman} , with three distinct frequency components at 2.18 THz, 2.85 THz, and 3.5 THz. In order to experimentally validate the theory discussed above, we multiply the transmitted THz field through the BBO with that induced by Raman pulse, $\phi_{THz}\phi_{Raman}$, as shown in Fig. 3c. Fig. 3d presents the absolute value of the 2D Fourier transformation of the data in Fig. 3c. By comparing Fig. 2b and Fig. 3d, one can clearly see that the measured signal of the BBO crystal using conventional EOS is dominated by the product field $\phi_{THz}\phi_{Raman}$ term, revealing a close agreement between the two signals in both time and frequency domains. Thus, this comparison provides conclusive evidence that the measured data for BBO is not a real $\chi^{(3)}$ signal; rather, it is a $\chi^{(2)}$ artifact due to imperfect balancing. It is worth noting that the same signal remains even by minimizing its size when trying to adjust θ as close as possible to 45° . Therefore, in 2D Raman-THz experiments involving non-centrosymmetric materials like BBO, where $\chi^{(2)}$ is nonzero, relying solely on the differential chopping scheme is insufficient to recover the desired third-order nonlinear signal.

C. Measurements at $\pm\theta$ around $\theta = 0^\circ$

In the previous section, we demonstrated both theoretically and experimentally that the measured signal in 2D Raman-THz experiments involving non-centrosymmetric samples is overwhelmingly dominated by second-order artifact. Here, to recover the extremely weak 3rd-order 2D Raman-THz response of the BBO crystal, we use the small bias detection scheme^{25–27}. In this scheme, the balanced difference signal is measured at opposite optical biases $\pm\theta$ where θ is a small angle of the quarter-wave plate close to 0° , as shown in Fig. 1c, right panel. A difference signal was calculated by subtracting these two consecutive measurements at each delay time. In that difference signal, the sign of $\sin(2\theta)$ coefficient flips, while the sign of $\cos^2(2\theta)$ coefficient remains unchanged (see equation 15). This is not the case for two measurements taken around 45° in the conventional EOS detection scheme. The real third-order nonlinear signal $S^{(3)}$ can thus be successfully recovered:

$$S^{(3)} = S(\phi, \theta) - S(\phi, -\theta) = \frac{2(1+T)}{\sin(2\theta)} \phi_{3rdNL}. \quad (18)$$

Figure 4a presents the 2D difference signal obtained by subtracting the time domain 2D signals measured at positive and negative optical biases, $\theta = \pm 2^\circ$. Figure 4b compares an 1D cut along t_1 axis at $t_2 = 0$ for the 2D difference signal (dotted blue line), with the signal that is dominated by the product field $\phi_{THz}\phi_{Raman}$ measured at positive optical bias (in red). It is important to note that these two data sets were extracted from the same measurement, enabling a meaningful comparison. The first observation is that the 2D difference signal ($\chi^{(3)}$ signal) is significantly weaker, by a factor of 20, compared to the $\chi^{(2)}$ artifact measured at opposite optical biases (see Fig. 4b).

More importantly, this clearly shows that the difference signal is shifted in phase compared to the $\chi^{(2)}$ artifact measured at positive optical bias. It is worth mentioning that imperfection in subtraction can never lead to a phase shift. To see the observed phase shift better we show in Fig. 4c the real part of the Fourier transformation of the 1D time domain cuts. A $\frac{\pi}{2}$ phase shift is clearly seen in this figure. The observed $\frac{\pi}{2}$ phase shift between the two time-domain signals indicates that they are generated through nonlinearities of different parity namely $\chi^{(2)}$ vs $\chi^{(3)}$, because each successive order of nonlinear interaction introduces a $\frac{\pi}{2}$ phase shift due to the complex nature of the nonlinear polarization.³⁰

The 2D Fourier transformation of the time domain data (Fig. 4a) is shown in Fig. 5b. The resulting 2D difference spectrum looks significantly different from the artifact 2D data shown in Fig. 2b. Specifically, it reveals a single round peak that is sharper and lacks any above-diagonal features. In order to assign this single peak, we measured both polarized Raman and THz transmission spectra of x-cut BBO, which are shown in Fig. 5a and Fig. 5c, respectively.

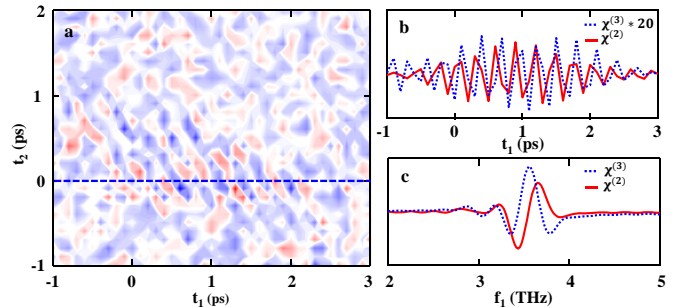


FIG. 4: a) Time-domain 2D Raman-THz data (2D difference signal) for the $100 \mu\text{m}$ thick x-cut BBO crystal obtained through the subtraction of the measured 2D signals at opposite optical biases. b) Comparison of 1D cuts along t_1 axis for the $\chi^{(2)}$ artifact measured at a positive optical bias (in red), and the $\chi^{(3)}$ signal (in blue), which is obtained through the subtraction of the measured signals at opposite optical biases. c) Fourier transformation of the 1D time domain cuts shown in panel (b), which highlights a distinct $\frac{\pi}{2}$ phase shift between the $\chi^{(3)}$ difference signal and the $\chi^{(2)}$ artifact.

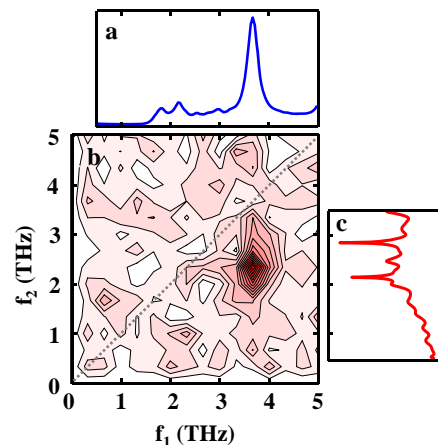


FIG. 5: a) Polarized Raman spectrum of x-cut BBO. b) Absolute value 2D spectrum of the 2D difference signal, $\chi^{(3)}$ signal, shown in Fig. 4a. c) THz transmission spectrum of x-cut BBO (sample oriented at 60° with respect to the polarization direction of the incident THz beam, since otherwise the absorbance of the THz modes would be too strong).

As can be seen from Fig. 5a, the polarized Raman spectrum of BBO reveals one strong peak at around 3.7 THz, which corresponds to the A_1 phonon mode of the BBO crystal and has been previously reported in the literature³¹. The THz transmission spectrum of BBO in Fig. 5c exhibits three distinct absorption features, a band at 2.15 THz which is assigned to A_1 mode, and two bands at 2.50 THz, and 2.85 THz which correspond to closely placed E and A_1 modes, in good agreement with the literature.^{31–33} The position of the peak along the f_1 frequency axis ($f_1 \approx 3.65$ THz) in the 2D spectrum

(Fig. 5b), coincides with A_1 phonon mode observed in the polarized Raman spectrum. The peak position along the f_2 frequency axis ($f_2 \approx 2.3$ THz) falls close to the position of the A_1 phonon mode observed at 2.15 THz in the THz transmission spectrum. Considering that the A_1 mode excited by the Raman pulse can only be coupled to the modes with the same symmetry this 2D spectrum suggests the presence of an anharmonic coupling between these two A_1 phonon modes within the BBO crystal. The small difference in the peak position along f_2 axis and the frequency of the A_1 phonon mode observed in the THz transmission spectrum is due to the fact that the convolution of the sample response with the IRF can shift the peak position along f_2 towards higher frequencies, as discussed in our previous work.¹⁹

IV. CONCLUSION

In conclusion, we have presented the 2D Raman-THz response of the x-cut BBO crystal, revealing a long-lived oscillatory feature along t_1 axis in the time-domain data. Our comprehensive data analysis demonstrated that the observed signal is dominated by a significant contribution from a second-order artifact due to imperfect balancing. Ignoring these second-order contributions can lead to misleading interpretations of the measured data. We showed both theoretically and experimentally that the third-order nonlinear response of the x-cut BBO crystal can be successfully recovered, effectively suppressing the strong artifact induced by the $\chi^{(2)}$ effect, through the application of the small bias detection scheme^{25–27}.

By implementing a bias detection scheme, we measured the signal at two small opposite optical biases around the zero angle of the quarter-wave plate. The resulting 2D difference signal, obtained by subtracting these two consecutive measurements, revealed a single round cross peak feature at $f_1 \approx 3.65$ THz and $f_2 \approx 2.3$ THz. These frequencies are in agreement with the frequency of two A_1 phonon modes of the BBO crystal, which are observed in the Raman and THz transmission spectra, respectively. Moreover, the observed $\frac{\pi}{2}$ phase shift between the 2D difference signal and the 2D signal measured at positive optical bias provides strong evidence that the 2D difference is indeed a $\chi^{(3)}$ signal. Therefore, our experimental findings suggest the presence of phonon-phonon coupling within the BBO crystal. Overall, the experimental approach presented here in signal recovery proves to be effective in disentangling the true third-order nonlinear response from the dominant artifact contribution arising from the $\chi^{(2)}$ process. This systematic approach can be applied to any other 2D THz spectroscopy experiments involving non-centrosymmetric samples, ensuring accurate data analysis and interpretation. This result paves the way for further expanding the applicability of 2D Raman-THz spectroscopy, thus facilitating the exploration of anharmonic phonon couplings in nonlinear crystals.

Acknowledgement: The work has been supported by the Swiss National Science Foundation (SNF) through the National Center of Competence and Research (NCCR) MUST as well by the MaxWater network of the Max Planck Society.

-
- ¹ W. Kuehn, K. Reimann, M. Woerner, and T. Elsaesser, *The Journal of Chemical Physics* **130**, 164503 (2009).
- ² M. Woerner, W. Kuehn, P. Bownan, K. Reimann, and T. Elsaesser, *New Journal of Physics* **15**, 025039 (2013).
- ³ T. Elsaesser, K. Reimann, and M. Woerner, *Concepts and Applications of Nonlinear Terahertz Spectroscopy* (Morgan & Claypool Publishers, 2019).
- ⁴ S. Houver, L. Huber, M. Savoini, E. Abreu, and S. L. Johnson, *Opt. Express* **27**, 10854 (2019).
- ⁵ M. Woerner, A. Ghalgau, K. Reimann, and T. Elsaesser, *The Journal of Chemical Physics* **154**, 154203 (2021).
- ⁶ S. Fleischer, R. W. Field, and K. A. Nelson, *Phys. Rev. Lett.* **109**, 123603 (2012).
- ⁷ J. Lu, Y. Zhang, H. Y. Hwang, B. K. Ofori-Okai, S. Fleischer, and K. A. Nelson, *Proceedings of the National Academy of Sciences* **113**, 11800 (2016).
- ⁸ J. Lu, X. Li, Y. Zhang, H. Y. Hwang, B. K. Ofori-Okai, and K. A. Nelson, *Two-Dimensional Spectroscopy at Terahertz Frequencies* (Springer International Publishing, 2019), pp. 275–320, ISBN 978-3-030-02478-9.
- ⁹ K. Reimann, M. Woerner, and T. Elsaesser, *The Journal of Chemical Physics* **154**, 120901 (2021).
- ¹⁰ C. Somma, K. Reimann, C. Flytzanis, T. Elsaesser, and M. Woerner, *Phys. Rev. Lett.* **112**, 146602 (2014).
- ¹¹ J. Lu, X. Li, H. Y. Hwang, B. K. Ofori-Okai, T. Kurihara, T. Suemoto, and K. A. Nelson, *Phys. Rev. Lett.* **118**, 207204 (2017).
- ¹² W. Kuehn, K. Reimann, M. Woerner, T. Elsaesser, and R. Hey, *The Journal of Physical Chemistry B* **115**, 5448 (2011).
- ¹³ W. Kuehn, K. Reimann, M. Woerner, T. Elsaesser, R. Hey, and U. Schade, *Phys. Rev. Lett.* **107**, 067401 (2011).
- ¹⁴ A. Liu and D. Ankit, arXiv preprint [arXiv:2405.00971](https://arxiv.org/abs/2405.00971) (2024).
- ¹⁵ J. Savolainen, S. Ahmed, and P. Hamm, *Proceedings of the National Academy of Sciences* **110**, 20402 (2013).
- ¹⁶ A. Shalit, S. Ahmed, J. Savolainen, and P. Hamm, *Nature chemistry* **9**, 273 (2017).
- ¹⁷ G. Ciardi, A. Berger, P. Hamm, and A. Shalit, *The Journal of Physical Chemistry Letters* **10**, 4463 (2019).
- ¹⁸ A. Shalit, S. J. Mousavi, and P. Hamm, *The Journal of Physical Chemistry B* **125**, 581 (2021).
- ¹⁹ S. J. Mousavi, A. Berger, P. Hamm, and A. Shalit, *The Journal of Chemical Physics* **156**, 174501 (2022), ISSN 0021-9606.
- ²⁰ I. A. Finneran, R. Welsch, M. A. Allodi, T. F. Miller, and G. A. Blake, *Proceedings of the National Academy of Sciences* **113**, 6857 (2016).

- ²¹ I. A. Finneran, R. Welsch, M. A. Allodi, T. F. Miller, and G. A. Blake, *The Journal of Physical Chemistry Letters* **8**, 4640 (2017).
- ²² G. Mead, H.-W. Lin, I.-B. Magdău, T. F. Miller, and G. A. Blake, *The Journal of Physical Chemistry B* **124**, 8904 (2020).
- ²³ B. E. Knighton, R. Tanner Hardy, C. L. Johnson, L. M. Rawlings, J. T. Woolley, C. Calderon, A. Urrea, and J. A. Johnson, *Journal of Applied Physics* **125**, 144101 (2019), ISSN 0021-8979.
- ²⁴ H.-W. Lin, G. Mead, and G. A. Blake, *Phys. Rev. Lett.* **129**, 207401 (2022).
- ²⁵ J. A. Johnson, F. D. J. Brunner, S. Grübel, A. Ferrer, S. L. Johnson, and T. Feurer, *J. Opt. Soc. Am. B* **31**, 1035 (2014).
- ²⁶ F. D. J. Brunner, J. A. Johnson, S. Grübel, A. Ferrer, S. L. Johnson, and T. Feurer, *J. Opt. Soc. Am. B* **31**, 904 (2014).
- ²⁷ P. Krauspe, N. Banerji, and J. Réhault, *J. Opt. Soc. Am. B* **37**, 127 (2020).
- ²⁸ S. Ahmed, J. Savolainen, and P. Hamm, *Review of Scientific Instruments* **85**, 013114 (2014).
- ²⁹ Y.-S. Lee, *Principles of terahertz science and technology*, vol. 170 (Springer Science & Business Media, 2009).
- ³⁰ R. W. Boyd, *Nonlinear optics* (Academic Press, 2008).
- ³¹ P. Ney, M. D. Fontana, A. Maillard, and K. Polgár, *Journal of Physics: Condensed Matter* **10**, 673 (1998).
- ³² J. Liu, X. Guo, J. Dai, and X.-C. Zhang, *Applied Physics Letters* **93**, 171102 (2008), ISSN 0003-6951.
- ³³ J. Liu and X. C. Zhang, *Journal of Applied Physics* **106**, 023107 (2009), ISSN 0021-8979.